

Nano-scale Characterization of White Layer in Broached Inconel 718

Zhe Chen ^{a,*}, Magnus Hörnqvist Colliander ^b, Gustav Sundell ^b, Ru Lin Peng ^a, Jinming Zhou ^c, Sten Johansson ^a, Johan Moverare ^a

^a Division of Engineering Materials, Linköping University, 58183 Linköping, Sweden

^b Department of Physics, Chalmers University of Technology, 41296 Gothenburg, Sweden

^c Division of Production and Materials Engineering, Lund University, 22100 Lund, Sweden

* Corresponding author Tel.: +46 13 281784 Fax: +46 13 282505 Email address: zhe.chen@liu.se

Abstract

The formation mechanism and properties of white layers created during broaching are not well investigated and understood to date. In the present study, multiple advanced characterization techniques with a nano-scale resolution, including transmission electron microscope (TEM), transmission Kikuchi diffraction (TKD), atom probe tomography (APT) as well as nano-indentation, have been used to systematically examine the microstructural evolution and corresponding mechanical properties of a surface white layer formed when broaching the nickel-based superalloy Inconel 718.

The TEM observations showed that the broached white layer consists of nano-sized grains, mostly in the range of 20 nm to 50 nm. The crystallographic texture detected by TKD further revealed that the refined microstructure is primarily attributed to strong shear deformation. Co-located Al-rich and Nb-rich fine clusters have been identified by APT, which are most likely to be γ' and γ'' clusters in a form of co-precipitates, where the clusters showed elongated and aligned appearance associated with the severe shearing history. The microstructural characteristics and crystallography of the broached white layer suggest that it was essentially formed by adiabatic shear localization in which the dominant metallurgical process is rotational dynamic recrystallization based on mechanically-driven subgrain rotations. The grain

refinement within the white layer led to an increase of the surface nano-hardness by 14% and a reduction in elastic modulus by nearly 10% compared to that of the bulk material. This is primarily due to the greatly increased volume fraction of grain boundaries when the grain size was reduced down to the nanoscale.

Keywords: Surface integrity, White layer, Broaching, Inconel 718, Adiabatic shear band, Mechanically-based subgrain rotation

1. Introduction

White layers have been identified at a variety of surfaces produced under diverse material removal processes or when subjected to wearing conditions. The white layer is a narrow band extending a few microns to several tens of microns from the surface, which appears metallographically featureless under the optical microscope due to its high resistance to etching.

Griffiths [1] suggested three main contributory mechanisms for white layer generation:

- (1) rapid heating and quenching which leads to transformation products;
- (2) surface reaction with the environment;
- (3) plastic flow which generates a homogeneous structure or one with a fine grain structure.

Surface white layers are mostly harder than the bulk material, but also they are brittle and normally accompanied by tensile residual stresses [2-4]. It has been recognized that the formation of a white layer is detrimental to the fatigue resistance; it eases the crack initiation/propagation, and therefore gives rise to a shorter fatigue life [5,6].

As the microstructure of the white layer could hardly be captured by optical and scanning electron microscopy (SEM), it is of necessity to employ X-ray diffraction (XRD) [2,7,8] or advanced characterization techniques, e.g. transmission electron microscopy (TEM) [2,9-13], atom probe tomography (APT) [2,3], etc. Nanocrystalline microstructure was frequently identified in white layers. Among the extensive studies in the case of hardened steels, martensite was found to develop if austenitization occurred due to extensive heat generation in the process

followed by rapid cooling [2,3,8]. Barry and Byrne [9] performed a TEM study on the surface white layer in turning of AISI 4340 steels with reinforced alumina tools. A surface white layer was formed when worn tools were used. Instead of the quenching effect which allows martensitic transformation, they found that there was only partially transformed material in the machined white layer, while the generation of this layer was essentially an adiabatic shear process as the similarity of the structure and crystallography in comparison with the adiabatic shear bands formed in martensitic steels when deformed at high strain rates. The dominant metallurgical process was perceived to be dynamic recovery.

Nickel-based superalloys are extensively used nowadays in the hot sections of turbine engines. Superior mechanical properties, together with the low thermal conductivity, however, lead to poor machinability of the alloys and consequently to a deteriorated machined surface [14]. When machining under abusive conditions, a surface white layer could be produced [15]. The microstructural features and formation mechanism of the white layer in machining nickel-based superalloys are studied less intensively. Wusatowska et al. [11] characterized the microstructure by TEM on a high speed milled surface of IN 100 alloys. It showed that the surface white layer is comprised of a great number of nano-grains, very likely due to dynamic recrystallization, and no apparent phase transformation occurred during the formation of the layer. When grinding cast IN738LC alloys with a high removal rate, Österle and Li [16] observed dissolution of the γ' phase and formation of a nanocrystalline structure in the superficial layer. Rapid heating to the melting temperature and subsequent quenching were suggested to take place and result in the distinct surface microstructure. Bushlya et al. [12] addressed issues in terms of white layer generation in high speed turning of aged Inconel 718. It was found that grain refinement occurred within the white layer, which is believed to be predominantly attributed to dynamic recrystallization and grain subdivision due to the severe plastic deformation. It has also been shown that all major phases of the alloy were present and there was no clear phase

transformation. In another study of machined Inconel 718 where micro-drilling was conducted [13], severe plastic deformation assisted by the high cutting temperature was proposed to be responsible for the formation of the white layer as elongated and sheared nano-grains were observed by TEM.

Previous studies have shown that white layer development and the mechanism behind its formation are strongly dependent on the material to be machined and the machining process specifically employed. Broaching is a high precision and productive final machining operation for manufacturing engineering components with a complex geometry, e.g., it is a method of choice to machine the complex-shaped slots on turbine discs. The presence of a white layer is certainly unfavorable because it impairs the resistance of the disc to fatigue failure. Greater insights to the microstructural characteristics and the mechanical properties of broached white layers are of significance if lifetime estimation is to be accurate for broached components. More importantly, a complete understanding is needed of the mechanism controlling the white layer formation during broaching in order to annihilate it on the broached parts. This is particularly the case for nickel-based superalloys which have a high tendency to form white layers in machining. Unfortunately, relevant investigations are reported rather infrequently despite that it has great practical importance.

Accordingly, the current work was undertaken to systematically examine the surface microstructural evolution and corresponding mechanical properties of broached Inconel 718 where a white layer was observed after the machining operation. Inconel 718 studied in this paper is a polycrystalline nickel-based superalloy which is widely used as a disc material in turbine engines. Most of the previous studies have introduced the observation of a nanocrystalline structure in surface white layers of machined Inconel 718 [12,13]. However, the mechanism of its generation was not well interpreted because typically only a single characterization approach, mostly TEM, was applied. A better understanding of this issue,

particularly in the case of broaching, has yet to be achieved and it requires multiple approaches giving more insights to the microstructural evolution during the formation of the white layer. There is no doubt that the heavily deformed and refined microstructure make challenges for characterizations since the resolution of micrometers has certainly been insufficient. In the present study, transmission Kikuchi diffraction (TKD) and APT, in addition to TEM, were applied. The development of TKD in a scanning electron microscope enables orientation mapping of nanostructured metals with resolution down to nearly 2 to 5 nm [17] and in the present study allowed effective characterization of the crystallographic orientations of the nano-sized grains on the broached surface. In addition, APT delivers three-dimensional compositional information at atomic scale around 0.1 to 0.3 nm [18]; it successfully identified the presence of the γ' and γ'' clusters in the broached white layer and captured their distinct morphology compared with that shown in the undeformed bulk material. Based on the observed microstructural characteristics, the formation mechanism of the white layer during broaching of Inconel 718 and its similarity to adiabatic shear bands are discussed. Moreover, the surface mechanical properties were tested by nano-indentation and it showed strong relevance with the microstructural refinement occurring when the broached white layer was formed.

2. Experimental methods

2.1 Material

The material to be broached was taken from an Inconel 718 disc forging, and the chemical composition is given in Table 1. The forging was solution heat treated at 970 °C, and then air cooled to room temperature, followed by a two-stage ageing for 8 h at 720 °C and further for 8 h at 620 °C, finally air cooled to room temperature. The resulting hardness was 410 HB. The microstructure of the aged bulk material consists of equiaxed grains of the γ matrix, platelets of the δ -Ni₃Nb phase, and primary carbides NbC which are formed during the solidification, see

Fig. 1. The material is strengthened partly by γ' -Ni₃Al precipitates, but mostly by γ'' -Ni₃Nb precipitates [19]; they are both in nano-scale and coherent with the γ matrix.

2.2 Broached specimens

Notches were machined on the rim of the aged forging by using a broaching process similar to that typically used for manufacturing fir-tree root fixings in turbine disc production. High speed steel tools PM-T15 (65 to 67 HRC) were employed with a rake angle of 12°, clearance angle of 3° and rise-per-tooth of 0.066 mm, 0.054 to 0.038 mm, and 0.013 mm for roughing, semi-finishing, and finishing sections. The broaching tools were in a semi-worn condition which is defined from the industrial point of view as that the tool has been used for several broaching operations of discs, while it can still fulfill the requirement of the dimension tolerance. The cutting speed was constant at $V_c = 3$ m/min, and broaching oil as cooling lubricant was applied throughout the entire broaching operations.

Broached specimens were extracted by wire-cut electric discharge machining from the flank surface of the second tooth of the fir-tree notches, see Fig. 2, where turbine blades are tightly pressed against the disc due to centripetal forces. The contact surfaces were then cross sectioned parallel to the direction of broaching, mounted and fine polished for microstructural studies.

2.3 Microstructural characterization

One of the polished cross section was etched in a HF-based etchant (HF-2, H₂O₂-50, HCl-40, H₂O-8 in vol.) and examined under optical microscope for white layer inspection. The other one was examined under a Hitachi SU-70 SEM, operating at 1.5 kV to 20 kV, together with electron channeling contrast imaging (ECCI) to have an overview of the microstructure beneath the broached surface. ECCI is a powerful technique to capture deformation, damage and even dislocations in deformed alloys [20].

Thin foils for the examination of TEM and TKD and needle tips for the APT analysis of the surface white layer were prepared from the polished cross section by the site-specific lift-out

procedure using a FEI Versa3D Lovac dual-beam focused ion beam/scanning electron microscope (FIB/SEM) instrument. TEM observation was conducted in an FEI Titan 80-300 operated at 300 kV. TKD investigations were performed using a Zeiss Leo 55 FEG-SEM operating at 20 kV equipped with a Bruker EDAX EBSD system consisting of an eFlash detector with a dedicated OPTIMUS TKD head and ESPRIT 2 software. The obtained data were analyzed using the MTEX package for Matlab [21]. For APT analysis, an Imago LEAP 3000X HR instrument was used, operated at 50 K under laser pulsing mode with a laser energy of 0.25 nJ and 200 kHz pulse frequency. Target evaporation rate was 0.5% ions per pulse. Reconstructions of isosurfaces were achieved using the Imago IVAS 6.8 software, with radius evolution estimated from TEM micrographs of the tips.

2.4 Nano-indentation

On the polished cross section, a matrix of ten indentations was performed in the regions away from the broached edge to measure the mechanical properties for the undeformed bulk material. However, when making indentations approaching to the superficial regions, the edge effect may reduce the accuracy of the measurements. In order to avoid this effect, another matrix of ten indentations was performed on the broached white layer from the top of the contact surface which has been mechanically fine polished using 0.25 μm polishing suspensions to remove the surface roughness. A notch with a side perpendicular to the polished surface was prepared by FIB at the region where the indentations were made. The residual thickness of the white layer and the appearance of the indents were then examined under SEM. The nano-indentation tests were conducted on the NanoTest Vantage system with a loading range of 0.01 to 500 mN. A Berkovich diamond indenter with a tip radius of 120 nm was used in the tests. Load control mode was applied and the load level was set to be 20 mN with loading rate of 5 mN/s and 30 s of holding time. The nano-hardness and elastic modulus for each indentation can be determined from the recorded load versus displacement curves [22].

3. Results

3.1 Microscopy

Fig. 3(a) shows an optical micrograph of the etched cross section. A thin band with a white featureless contrast was observed on the broached surface, the thickness is only 2 to 3 μm on average. When examined in SEM, this band showed a high resistance to the etching, see Fig. 3(b), which confirms the appearance of a white layer. The ECCI micrograph in Fig. 4(a) captures the highly deformed microstructure beneath the broached surface. Despite that the structure of the surface white layer is still not fully resolved, one could clearly see from Fig. 4(b) that the plate-like δ particles were heavily deformed and fragmented due to the effect of deformation breakage [23]. In the near surface region, shearing and elongation of grains, grain boundaries and δ phase occurred towards the broaching direction. The intensity of the plastic deformation is reduced as the increased depth. More detailed characterization of the sub-surface microstructure and the nano-hardness depth profile can be found in [24].

To clarify the internal structure of the surface white layer induced by broaching, a thin foil was produced from the polished cross section, with the foil plane lying in the transverse-normal plane, and examined under TEM. Fig. 5 shows the bright-field micrographs where the appearance of the surface structure is revealed. It consists of ultra-fine equiaxed grains, while the majority of the grains are in the order of several tens of nanometers (approx. 20 nm to 50 nm). Deformed and fragmented δ particles were previously observed in SEM to distribute in the white layer, but they are locally absent in the selected area where the TEM foil is prepared. The presence of other precipitates, e.g., γ' and γ'' which commonly exist in aged Inconel 718 as shown in Fig. 1, can also hardly be identified in the bright-field images.

3.2 Texture analysis

TKD investigations were performed in order to study whether the highly refined grains are a consequence of the surface deformation during broaching, or if new grains have been created

by recrystallization processes. Another thin foil was extracted in the broaching-transverse plane such that the entire foil only contains the regions of the broached white layer. Consistent with the TEM observations, the crystallographic orientation map and band contrast map, as shown in Fig. 6, also imaged the ultra-fine structure of the broached white layer. The number of un-indexed pixels is relatively high. This could be due to the deformed and refined structure as well as the presence of small precipitate particles (see Section 3.3) which reduced the quality of the Kikuchi diffraction patterns; the un-indexed regions in Fig. 6(a) generally correspond to the dark areas in the band contrast map (Fig. 6(b)) where the recorded pattern quality is poor. Nevertheless, the indexing rate, approximately 40%, is sufficient for the texture analysis, and the unprocessed data were used to ensure the absence of artefacts from the noise reduction. The (111) and (110) pole figures collected from the foil plane and the 90° rotational plane, i.e. broaching-normal plane, are presented in Fig. 6(c) and (d); they correlate well with the previous observations by other authors [25,26], based on XRD pole figure measurement, on machined Inconel 718 and coppers, which show the presence of a shear-induced deformation texture, typical of face-centered cubic (FCC) materials.

Fig. 7 shows $\varphi_2 = \text{constant}$ (0° to 90° in steps of 15°) sections of the orientation distribution function (ODF) corresponding to Fig. 6(d). The main ideal orientations in simple shear deformation of FCC materials are found to be distributed along the two fibers, $\{111\}\langle uvw \rangle$ fiber (or $\{111\}$ fiber in short) and $\{hkl\}\langle 110 \rangle$ fiber (or $\langle 110 \rangle$ fiber in short) [27-29]. To aid in the analysis of the texture characteristics in the broached white layer, the Euler angles of these ideal orientations [30] are shown in Table 2 and their locations are marked on Fig. 7. It shows that in general the experimentally observed texture can be described by the ideal orientations associated with simple shear, but there is a rotation with respect to the exact positions. As suggested by Saiyi et al. [31], this rotation primarily results from the deviation of deformation from simple shear along the shear plane due to, for example, the cutting force

component normal to this plane or the material strain hardening. The texture components can be denoted as $A_{1\theta}^*$, $A_{2\theta}^*$, A_θ , \bar{A}_θ , B_θ , \bar{B}_θ , and C_θ with subscript θ indicating the rotation from the simple shear texture. For the formation of the texture in the broached white layer, the C_θ component appears to be dominant followed by B_θ and \bar{B}_θ , while the component $A_{2\theta}^*$ is absent. The preferred orientations are concentrated along three dominant fibers, designated as f_1 , f_2 and f_3 ; these fibers have also been seen in equal channel angular extrusion and plane strain machining of coppers [26,31] where the f_1 fiber was identified to solely consist of the rotated $\{111\}$ partial fiber (or $\{111\}_\theta$ partial fiber), the f_2 fiber includes the rotated $\langle 110 \rangle$ partial fiber (or $\langle 110 \rangle_\theta$ partial fiber) as well as the $\{111\}_\theta$ partial fiber, and the f_3 fiber, which is symmetrical with respect to the f_2 fiber, again contains both the $\langle 110 \rangle_\theta$ partial fiber and the $\{111\}_\theta$ partial fiber. It can be clearly seen that the major texture components and fibers as identified by TKD in the broached white layer are strongly correlated with those for simple shear deformation.

By using in-situ image correlation, it has been shown that the material in the surface layer underwent simple shear deformation during plane strain machining of OFHC-Cu [26], and the visco-plastic self-consistent (VPSC) model could qualitatively reproduce the experimentally observed textures using grain-splitting and co-rotation schemes. In the present study, the application of simple shear deformation in VPSC [32], starting from 1000 grains with uniform crystallographic orientations, resulted in textures qualitatively similar to that obtained from the TKD investigations, while the best agreement was obtained using the secant interaction model, which produced sharp textures compared to alternatives, however, the fine scale details could not be completely reproduced. Shear strains, γ , in the order of 4 to 5, were imposed with the purpose of reproducing the significantly higher intensity of the texture component C_θ compared to the $A_{1\theta}^*$ on the $\varphi_2 = 0^\circ$ section in Fig. 7. This also yielded texture indexes close to the experimentally observed values, nearly 2.27, as seen in Fig. 6(c) and (d). Fig. 8 shows the simulated ODF by VPSC after simple shear deformation to a shear strain, $\gamma = 4$. The three

dominant fibers f_1 , f_2 and f_3 that have been identified in the experimentally observed texture were successfully reproduced by VPSC simulations. However, there is an almost complete absence of the $B_\theta / \bar{B}_\theta$ components in the $\varphi_2 = 45^\circ$ section, contrary to the experimental observations. Employing grain splitting, co-rotation schemes or more advanced grain interaction models did not improve the situation. Basu et al. [26] did not report detailed comparisons between the experimental results and the VPSC simulations for OFHC-Cu, thus it is currently not possible to say if the present discrepancies are a result of material behavior or due to that the deformation model of simple shear is oversimplified. Besides, the rotation of the texture components shown in the experimental ODF with respect to the ideal orientations of the simple shear texture was not observed in the simulated ODF due to the simplified deformation model. Nevertheless, the qualitative match of the two ODFs still offers evidence that the crystallographic texture in the broached white layer was developed in strong relation with severe shear deformation.

The low indexing rate during TKD did not permit sufficient clean-up to allow calculation of correlated misorientation distributions. However, Fig. 9 presents the uncorrelated distribution histogram from the TKD data, as well as the purely texture-induced misorientation distribution (solid line) calculated from the ODF corresponding to Fig. 7 without a consideration of any spatial correlations. These agree very well, indicating that there is no particular spatial correlation in the TKD data. It implies that the grain boundaries formed in the broached white layer are high-angle boundaries, since adjacent grains belong to random fibers of the shear texture. The deviation of the two distributions from the Mackenzie distribution [33] for a FCC polycrystal with random textures and no orientation preference between neighboring grains (dash line) is caused by the overrepresentation of angles corresponding to the misorientations between the different texture fibers [34]. The finding suggests that the grain refinement accompanied by a strong texture evolution led to a significantly misoriented sub-grain structure

in the broached white layer. The mechanism for the formation of the high-angle boundaries will be discussed in the subsequent Section 4.1 based on the dominant metallurgical process occurring during the generation of the white layer.

3.3 APT investigations

APT analysis was conducted to investigate the presence of precipitates, e.g. γ' and γ'' on the nano-scale, within the surface white layer. The needles were lift-out in the broaching-transverse plane with the analysis direction in the transverse direction. Fig. 10 shows a reconstruction viewed from two directions, rotated 90° around the long axis. It contains isosurfaces corresponding to 4.5 at.% of Al and Nb, where nano-sized Al-rich and Nb-rich clusters can be observed, typically located in the vicinity of each other. The low isoconcentrations were chosen in order to visualize the relatively small particles, but as a consequence the size of the larger particles was greatly overestimated. In addition, the local magnification effect due to the different evaporation fields between the matrix and particles leads to trajectory overlaps close to the interface which in turn could also give rise to overestimations of the particle size up to a factor of two in nickel-based superalloys [35].

The composition gradients across the interfaces of the clusters and the γ matrix are given as proximity histograms (proxigrams) in Fig. 11. The atoms partitioned in the two types of clusters are respectively relevant formers of the γ' and γ'' precipitates. It should be noted that the isosurfaces were reconstructed with the 27 Da peak assigned to $^{27}\text{Al}^+$, without a consideration of the overlap with $^{54}\text{Fe}^{2+}$ and $^{54}\text{Cr}^{2+}$. This is not an issue for visualizing the clustering of Al, but will affect the chemical quantification in the proxigrams. The chemistry is quantitatively accurate only on the positive side of the interface, i.e. the “inner” part of the clusters since neither Fe nor Cr is expected to partition to any of the γ' and γ'' precipitates. Outside the isosurfaces the $^{54}\text{Fe}^{2+}$ and $^{54}\text{Cr}^{2+}$ will be identified as Al, resulting in an overestimation of the Al concentration and an underestimation of the Fe and Cr concentration. This also makes the

composition change over the interface more diffuse than the actual gradient. It is, however, not a major effect as the natural abundance of the ^{54}Fe and ^{54}Cr isotopes is low (5.8% and 2.3%, respectively), whereas ^{27}Al is the only Al isotope.

Despite that quantitative chemical analysis of very small objects is by necessity associated with uncertainty, optimized analyses of the cluster compositions were achieved by focusing on single large Al and Nb rich regions, for which more conservative isosurfaces, i.e. using higher Al and Nb isoconcentrations, were reconstructed as an attempt to avoid the influence of composition gradients around the interface. As a result, the “inner” part of the regions was then selected and analyzed by a peak decomposition based on the natural abundance of isotopes. The quantitative compositions of the selected clusters are illustrated in Table 3, which are, to a large extent, in accordance with the compositions for γ' and γ'' as measured by APT in the undeformed bulk material. Hence, the two types of clusters detected in the surface white layer are very likely corresponding to the γ' and γ'' precipitates and it appears that they were co-precipitated in the microstructure.

3.4 Mechanical properties

Fig. 12(a) shows the distinct mechanical properties of the broached white layer. It exhibits an increased nano-hardness and a reduced elastic modulus compared with the values obtained from the undeformed bulk material. One concern with the measurements was that the fine mechanical polishing from the top of the broached contact surface caused reduction of the thickness of the white layer. When examined in SEM, the cross sectional observation from the notch prepared by FIB showed that the residual thickness is slightly above 2 μm at the region where the indentations were made, see Fig. 12(b). According to the recorded load versus displacement curves, as shown in Fig. 12(c), with the applied load of 20 mN, the indenter penetrated the white layer to a depth with a maximum $h_{\text{max}} = 370$ nm, exceeding the threshold of 10% with respect to the white layer thickness remained after polishing, but certainly in a reasonable range for

nano-indentation measurements. The indents left on the broached white layer showed a symmetrical triangle shape, see for example in Fig. 12(d), which also indicates that the result shown in Fig. 12(a) is reliable. However, nano-indentation is a local test method, as one can see from Fig. 12(d) that a larger indent (the middle indent) was created when the indenter was located at the region where δ particles are present. Hence, the measured nano-hardness and elastic modulus showed a large scatter due to the inhomogeneity of the microstructure.

4. Discussions

This is the first attempt to systematically describe the microstructural and mechanical characteristics of a white layer formed during broaching. The characterizations were performed on scales from a few microns down to tens of nanometers. The observed microstructural evolution provide insights into the mechanism for the formation of the white layer. In this section, it will be discussed in detail. In addition, the distinct mechanical properties of the broached white layer associated with the nanocrystalline surface structure will also be discussed.

4.1 Mechanism of white layer formation

Significant refinement of the microstructure with nano-sized grains has been observed in the white layer generated on the broached surface, see Fig. 5, while the TKD analysis, as shown in Fig. 6 and 7, further indicates that the formed microstructure seems to be primarily attributed to strong shear deformation. Similar grain appearance and texture were observed by TKD in the primary shear zone in Inconel 718 chips from machining, as well as in adiabatic shear bands from dynamic shear tests [36]. Despite that the grain size is relatively small, and the formed texture seems to be slightly rotated, due to differences of the deformation and temperature history, the microstructure and crystallographic orientation within the broached white layer are highly comparable with the features characterized in [36]. This suggests that the formation of the white layer during broaching essentially is a consequence of adiabatic shear localization on

the broached surface. This is further supported by the observations of the sharp interface between this superficial layer and the sub-surface regions, as seen in Fig. 4(a).

The adiabatic instability of plastic flow in shear takes place when the generated heat due to the plastic work has insufficient time to dissipate into the surrounding material [37]. Once the thermal softening exceeds the strain and strain rate hardening, because of the locally reduced material strength, the plastic deformation will become unstable and give way to continued shear deformation to a narrow band, which is often referred to as adiabatic shear bands. Numerous studies have shown that machined white layers appeared when cutting at high speeds, without external cooling or using worn tools [9,11,12,38]. Under such aggressive conditions, giant heat and consequently an increased temperature is created on the machined surface due to the large plastic work, high strain rate and the intense friction [39].

Although the tendency for adiabatic shear localization increases when materials are deformed at high strain rates, the present study shows that it could happen even when the cutting speed is as low as 3 m/min depending on the machining process applied and the material to be machined. Broaching is a multipoint cutting method, i.e. there are always at least two, preferable more cutting edges in contact with the surface at any time, while each cutting edge can act as an independent heat source [39] during the process. The usage of the broaching oil can contribute to lowering the friction, dissipating the heat, thereby reducing the global cutting temperature. However, materials like Inconel 718 are prone to be subjected to considerable plastic work due to the high strength and a great temperature gradient could be created on the machined surface as a result of the low thermal conductivity. Klocke et al. [40] collected the surface temperature signals when broaching Inconel 718 using high speed steel tools and the analysis revealed that the cutting temperature could exceed 700 °C despite relatively low cutting speeds, ranging from 2.5 m/min to 10 m/min and the use of a cooling lubricant. Due to the temperature gradient, the cutting process becomes localized on the machined surface, and it will in turn lead to more

significant local temperature rise, thereby enhancing the surface material softening, which eventually results in continued shear localization. More localized cooling techniques, which are applied directly to the cutting tool/workpiece interface instead of using conventional flood coolant, e.g., high pressure cooling or minimum quantity lubrication, are very likely to be beneficial to prevent the formation of white layers in broaching since they can more effectively reduce the local temperature rise on the broached surface and retard the occurrence of shear localization. This effect is of great interest for further studies in the future.

Material softening during deformation is attributed to microstructural changes by which dislocations realign and eliminate each other allowing the material to accommodate larger plastic work. The dominant mechanisms can be divided into two categories: dynamic recovery and dynamic recrystallization; they are generally regarded as competing processes [41,42]. McQueen [43] pointed out that alloys with low stacking fault energies, in which dynamic recovery is sluggish, are more likely to undergo dynamic recrystallization. On this basis, Bushlya et al. [12] proposed that dynamic recrystallization and grain subdivision primarily contributed to the structural refinement observed in the white layer on high-speed turned Inconel 718.

There are several nucleation mechanisms for recrystallization that have been proposed and examined. One of the two classical theories was proposed by Bailey and Hirsch [44], known as strain induced boundary migration, and the other one is based on the process of subgrain coalescence, first proposed by Li [45]. Microstructural characterization conducted by Wang et al. [46] in the hot deformed Inconel 718 at temperatures from 950 °C to 1120 °C with a relatively low strain rate of 10^{-1} s^{-1} substantiated the presence of dynamically recrystallized grains under the combined mechanism of boundary migration and subgrain rotation. However, studies by Hines et al. [47,48] suggested that conventional diffusion-based recrystallization mechanisms were inadequate to account for the observed recrystallized grains in the copper

adiabatic shear bands as the kinetics is too slow compared with the shear band cooling rate, and therefore a mechanically-driven subgrain rotation mechanism was established. Such a rotational form of dynamic recrystallization has also been suggested by other authors to explain the observed microstructural evolution in the localized shear bands formed during high strain, high strain rate deformation processes [36,41,49].

Given the dominant texture fibers identified in the broached white layer, see Fig. 7, diffusion controlled recrystallization was less likely to happen in the present case since the cube texture [50] is commonly created after annealing of heavily deformed FCC materials during which the thermally activated recrystallization usually takes place. Instead, these texture fibers show that the nano-sized grains were created by deformation induced grain subdivision with large lattice rotations, driving the $\{111\}$ plane parallel to the shear plane, i.e. the broaching-transverse plane, and the $\langle 110 \rangle$ direction aligned with the shear direction, i.e. the broaching direction. Although the deformation rate was relatively slow due to the low broaching speed, the amount of the plastic strain imposed on the surface material is presumably considerable. The original grains were heavily sheared and elongated, subdivided, and rotated as the deformation continued to take place. The formation of the shear texture is due to rotations of the equiaxed sub-grains once the strain accommodation cannot be achieved by grain subdivision. Meanwhile, increasingly higher misorientation angles were developed between the sub-grains since they rotated at different rate and with different rotation axes, as suggested by Hughes and Hansen [51]. The development of high-angle grain boundaries is evident from the analysis of the uncorrelated distribution histogram shown in Fig. 9. The microstructural evolution described herein based on the characterized features in structure and crystallography of the broached white layer is greatly consistent with the mechanically-based subgrain rotation mechanism reported in [47,48]. The final stage of this rotational dynamic recrystallization is boundary refinement during the subsequent cooling through dislocation annihilation by dislocation climb

[48]. Recrystallized grains with faceted, high-angle boundaries will form if there is sufficient time for this process to occur. In the present study, one may have noted that the boundaries of the equiaxed nano-grains formed on the broached surface are mostly unfaceted, see Fig.5. This could be due to either the short cooling time as the use of coolant and heat conduction to the bulk, or the increased difficulties for dislocation climb in Inconel 718 by the presence of solute atoms and precipitates. Despite that the boundary refinement appears to incompletely take place at the final stage during the formation of the broached white layer, overall, the steps that constitute the rotational dynamic recrystallization on the basis of mechanically-driven subgrain rotations can successfully account for the microstructural evolution taking place within this localized surface shear band.

4.2 γ' and γ'' precipitates in white layer

An interesting observation from the present study is that the γ' and γ'' appears to be present in a form of co-precipitates in the broached white layer which was developed as an adiabatic shear band. Precipitate shearing is an important mechanism in Inconel 718 when subjected to large deformation, during which the strengthening precipitates would be sheared and fragmented into slices, while with the increase of the plastic strain, the γ' and γ'' precipitates were observed to disappear in the deformation bands [52]. Considering the large plastic strain, coupled with temperature rise on the broached surface due to the nature of the adiabatic shearing, a possible explanation for the formation of this observed microstructure is that the γ' and γ'' particles have been dissolved during broaching, either by severe precipitate shearing or by thermal impacts, but subsequently they were re-precipitated during cooling.

The precipitate structure in the undeformed bulk is presented in Fig. 13. The isosurfaces in Fig. 13(a) were chosen to best visualize the precipitate particles, but are prone to the same uncertainties in concentration as discussed previously. It can be clearly seen from Fig. 13(a) that the γ' and γ'' are generally co-precipitated in the bulk material (a magnified view of two

such particles are shown in Fig. 13(d)). The γ'' precipitates are favorable to nucleate at the γ' / γ matrix interfaces, stacking (001) γ'' over one of the three {001} γ' planes [53,54]. If the Al and Nb isosurfaces are plotted separately, see Fig. 13(b) and (c), it becomes obvious that there is a depletion of γ'' in the upper left corner. A closer inspection also reveals that the γ' particles are more spherical in this region, as a result of the absence of co-precipitation. This is presumably due to the presence of a large δ particle just outside the reconstructed volume, leading to local Nb depletion. The lower Nb concentration in this region was verified by concentration profiles through the reconstructed volume. Comparing with the morphology of the γ' and γ'' particles from the undeformed bulk, the Al-rich and Nb-rich clusters within the broached white layer shows a distinctly different morphology. The shape is very flat, almost in two dimensions like a plate, and in many cases elongated into nearly linear features. The clusters are also aligned in the microstructure, as can be seen from the rotated isosurface maps in Fig. 10. Despite that the direction of broaching cannot be identified during the reconstruction, it is not far-fetched to assume that the alignment of the clusters is a result of the directionality due to severe shearing. The morphology of the clusters shows strong relation to the deformation history, but this does not necessarily rule out the dissolution/re-precipitation mechanism. If there was insufficient time for solute diffusion and re-distribution during the subsequent cooling, the γ' and γ'' clusters could have re-precipitated with inheritance of the elongated and orientated appearance. Most of the clusters are significantly fine even though a relatively low isoconcentration was chosen in Fig. 10 in comparison with the size of the γ' and γ'' precipitates in the bulk material as shown in Fig. 13(a). It could be a result of either the fragmentation of the precipitates during broaching or the early stage of precipitation due to the rapid cooling. Nevertheless, the co-precipitation of the Al-rich and Nb-rich clusters is evident, consistent with previous observations that γ' and γ'' are co-precipitated in Inconel 718 even in the earliest stage of aging [53,54]. However, from

the current study, it cannot fully resolve the underlying mechanism behind the formation of the nano-precipitates in the broached surface microstructure. This is worth clarification in the future.

4.3 Mechanical properties of white layer

It has been shown that the generation of the broached white layer enhances the surface nano-hardness up to 14% for which the primary reason is believed to be the grain refinement of the surface microstructure. Saoubi et al. [55] reported that the surface hardness improvement was not remarkable for Alloy 718 as it showed in the case of other superalloys developed with better mechanical performances at higher operating temperatures, like Alloy 720Li and especially RR 1000, when subjected to abusive drilling operation with the same conditions. The maximum nano-hardness value appeared within the superficial white layer by a comparable 12% increase from the plateau deeper into regions of the bulk material. With a reduction of the grain size down to nanoscale, as seen in Fig. 5, the volume fraction of grain boundaries is largely increased and the mechanical properties of the broached white layer is influenced by increased difficulties in forming and moving dislocations. Schiøtz and Jacobsen [56] further suggested, based on the simulation work in Cu, that the peak strength or hardness in nanocrystalline microstructure occurs at a critical grain size corresponding to the transition in the microscopic deformation mechanism from dislocation-mediated plasticity to grain boundary sliding.

The grain refinement in the white layer, however, reduces the surface elastic modulus by nearly 10%. This elastic softening is also associated with the fact that grain boundaries occupy a larger fraction of the total volume on the broached surface with the smaller grain size. The weak bonding of atoms at grain boundaries and triple junctions certainly has a deleterious effect for the elastic modulus [57].

5. Conclusions

The formation of a machined white layer is material, process and cutting variable sensitive. The present study clearly shows that it could be created during broaching of Inconel 718 as an

adiabatic shear band even if a coolant was applied and machining operation was performed under a relatively low strain rate at a cutting speed as low as 3 m/min.

The broached white layer consists of a nanocrystalline structure with a strong shear texture, while the majority of the grains are in the range of 20 nm to 50 nm. The microstructural characteristics and crystallography of the broached white layer suggest that it is essentially formed by adiabatic shear localization in which the dominant metallurgical process is rotational dynamic recrystallization based on mechanically-driven subgrain rotations.

Co-located Al-rich γ' and Nb-rich γ'' nano-clusters have been identified in the broached white layer. Both of these two types of clusters have elongated and aligned appearance as influenced by the severe shear deformation history.

The grain refinement within the white layer increases the surface nano-hardness by 14%, but causes a reduction almost up to 10% in elastic modulus compared to that of the bulk material. This is due to the greatly increased volume fraction of grain boundaries when the grain size reduces down to the nanoscale.

Acknowledgements

The authors would like to acknowledge A. Billenius from Linköping University for the help with the laboratory work, A.H.S. Iyer, H. Lai and H. Pettersson at Chalmers for performing the FIB, TEM and TKD work. Siemens Industrial Turbomachinery AB, ÅForsk Foundation grant 15-334 and Faculty grant SFO-MAT-LiU#2009-00971 are also greatly acknowledged for their valuable supports in this study.

References

- [1] B. Griffiths, Mechanisms of white layer generation with reference to machining and deformation processes, *J. Tribol.* 109 (1987) 525-530.
- [2] H. Zhang, S. Ohsaki, S. Mitao, M. Ohnuma, K. Hono, Microstructural investigation of white etching layer on pearlite steel rail, *Mater. Sci. Eng. A.* 421 (2006) 191-199.
- [3] J. Takahashi, K. Kawakami, M. Ueda, Atom probe tomography analysis of the white etching layer in a rail track surface, *Acta Mater.* 58 (2010) 3602-3612.

- [4] R.L. Peng, J. Zhou, S. Johansson, A. Bellinius, V. Bushlya, J. Stahl, Residual stresses in high speed turning of nickel-based superalloy*, *HTM Journal of Heat Treatment and Materials*. 69 (2014) 46-53.
- [5] Y. Guo, D.W. Schwach, An experimental investigation of white layer on rolling contact fatigue using acoustic emission technique, *Int. J. Fatigue*. 27 (2005) 1051-1061.
- [6] D.W. Schwach, Y. Guo, A fundamental study on the impact of surface integrity by hard turning on rolling contact fatigue, *Int. J. Fatigue*. 28 (2006) 1838-1844.
- [7] S. Veldhuis, G. Dosbaeva, A. Elfizy, G. Fox-Rabinovich, T. Wagg, Investigations of white layer formation during machining of powder metallurgical Ni-based ME 16 superalloy, *J. Mater. Eng. Perform.* 19 (2010) 1031-1036.
- [8] J. Kundrák, Z. Gácsi, K. Gyáni, V. Bana, G. Tomolya, X-ray diffraction investigation of white layer development in hard-turned surfaces, *Int. J. Adv. Manuf. Technol.* 62 (2012) 457-469.
- [9] J. Barry, G. Byrne, TEM study on the surface white layer in two turned hardened steels, *Mater. Sci. Eng. A*. 325 (2002) 356-364.
- [10] Y. Xu, L. Fang, Q. Cen, J. Zhu, Nano structure and transformation mechanism of white layer for AISI1045 steel during impact wear, *Wear*. 258 (2005) 537-544.
- [11] A. Wusatowska-Sarnek, B. Dubiel, A. Czyrska-Filemonowicz, P. Bhowal, N.B. Salah, J. Klemberg-Sapieha, Microstructural characterization of the white etching layer in nickel-based superalloy, *Metall. Mater. Trans. A*. 42 (2011) 3813-3825.
- [12] V. Bushlya, J. Zhou, F. Lenrick, P. Avdovic, J. Ståhl, Characterization of white layer generated when turning aged Inconel 718, *Procedia Eng.* 19 (2011) 60-66.
- [13] M. Imran, P.T. Mativenga, A. Gholinia, P.J. Withers, Evaluation of surface integrity in micro drilling process for nickel-based superalloy, *Int. J. Adv. Manuf. Technol.* 55 (2011) 465-476.
- [14] E.O. Ezugwu, Key improvements in the machining of difficult-to-cut aerospace superalloys, *Int. J. Mach. Tools Manuf.* 45 (2005) 1353-1367.
- [15] D. Ulutan, T. Ozel, Machining induced surface integrity in titanium and nickel alloys: A review, *Int. J. Mach. Tools Manuf.* 51 (2011) 250-280.
- [16] W. Österle, P. Li, Mechanical and thermal response of a nickel-base superalloy upon grinding with high removal rates, *Mater. Sci. Eng. A*. 238 (1997) 357-366.
- [17] P.W. Trimby, Y. Cao, Z. Chen, S. Han, K.J. Hemker, J. Lian, X. Liao, P. Rottmann, S. Samudrala, J. Sun, Characterizing deformed ultrafine-grained and nanocrystalline materials using transmission Kikuchi diffraction in a scanning electron microscope, *Acta Mater.* 62 (2014) 69-80.

- [18] T.F. Kelly, M.K. Miller, Atom probe tomography, *Review of Scientific Instruments*. 78 (2007) 031101.
- [19] D. Paulonis, J. Oblak, D. Duvall, Precipitation in nickel-base alloy 718, *Trans. Quart. ASM*. 62 (1969) 611-622.
- [20] J.J. Moverare, S. Johansson, R.C. Reed, Deformation and damage mechanisms during thermal-mechanical fatigue of a single-crystal superalloy, *Acta Mater*. 57 (2009) 2266-2276.
- [21] F. Bachmann, R. Hielscher, H. Schaeben, Texture analysis with MTEX-free and open source software toolbox, *Solid State Phenomena*. 160 (2010) 63-68.
- [22] J. Zhou, V. Bushlya, P. Avdovic, J.E. Ståhl, Study of surface quality in high speed turning of Inconel 718 with uncoated and coated CBN tools, *Int. J. Adv. Manuf. Technol*. 58 (2012) 141-151.
- [23] H. Zhang, S. Zhang, M. Cheng, Z. Li, Deformation characteristics of δ phase in the delta-processed Inconel 718 alloy, *Mater. Charact*. 61 (2010) 49-53.
- [24] Z. Chen, R.L. Peng, J. Moverare, P. Avdovic, J. Zhou, S. Johansson, Surface integrity and structural stability of broached Inconel 718 at high temperatures, *Metall. Mater. Trans. A*. 47 (2016) 3664-3676.
- [25] R. M'Saoubi, T. Larsson, J. Outeiro, Y. Guo, S. Suslov, C. Saldana, S. Chandrasekar, Surface integrity analysis of machined Inconel 718 over multiple length scales, *CIRP Annals-Manuf. Technol*. 61 (2012) 99-102.
- [26] S. Basu, M.R. Shankar, Crystallographic textures resulting from severe shear deformation in machining, *Metall. Mater. Trans. A*. 46 (2015) 801-812.
- [27] G. Canova, U. Kocks, J. Jonas, Theory of torsion texture development, *Acta Metall*. 32 (1984) 211-226.
- [28] F. Montheillet, M. Cohen, J. Jonas, Axial stresses and texture development during the torsion testing of Al, Cu and α -Fe, *Acta Metall*. 32 (1984) 2077-2089.
- [29] L. Tóth, P. Gilormini, J. Jonas, Effect of rate sensitivity on the stability of torsion textures, *Acta Metall*. 36 (1988) 3077-3091.
- [30] S. Li, I.J. Beyerlein, M.A. Bourke, Texture formation during equal channel angular extrusion of fcc and bcc materials: comparison with simple shear, *Mater. Sci. Eng. A*. 394 (2005) 66-77.
- [31] S. Li, I.J. Beyerlein, D.J. Alexander, S.C. Vogel, Texture evolution during multi-pass equal channel angular extrusion of copper: neutron diffraction characterization and polycrystal modeling, *Acta Mater*. 53 (2005) 2111-2125.
- [32] R. Lebensohn, C. Tomé, A self-consistent anisotropic approach for the simulation of plastic deformation and texture development of polycrystals: application to zirconium alloys, *Acta Metall. Mater*. 41 (1993) 2611-2624.

- [33] J. Mackenzie, Second paper on statistics associated with the random disorientation of cubes, *Biometrika*. 45 (1958) 229-240.
- [34] L. Toth, C. Gu, B. Beausir, J. Funderberger, M. Hoffman, Geometrically necessary dislocations favor the Taylor uniform deformation mode in ultra-fine-grained polycrystals, *Acta Mater.* 117 (2016) 35-42.
- [35] L. Viskari, K. Stiller, Atom probe tomography of Ni-base superalloys Allvac 718Plus and Alloy 718, *Ultramicroscopy*. 111 (2011) 652-658.
- [36] J. Johansson, C. Persson, H. Lai, M.H. Colliander, Microstructural examination of shear localisation during high strain rate deformation of Alloy 718, *Mater. Sci. Eng. A*. 662 (2016) 363-372.
- [37] S. Timothy, The structure of adiabatic shear bands in metals: a critical review, *Acta Metall.* 35 (1987) 301-306.
- [38] S. Bosheh, P. Mativenga, White layer formation in hard turning of H13 tool steel at high cutting speeds using CBN tooling, *Int. J. Mach. Tools Manuf.* 46 (2006) 225-233.
- [39] N. Abukhshim, P. Mativenga, M. Sheikh, Heat generation and temperature prediction in metal cutting: A review and implications for high speed machining, *Int. J. Mach. Tools Manuf.* 46 (2006) 782-800.
- [40] F. Klocke, S. Gierlings, D. Veselovac, Concept for temperature control in broaching nickel-based alloys, *Key Eng. Mater.* 523 (2012) 469-474.
- [41] M. Perez-Prado, J. Hines, K. Vecchio, Microstructural evolution in adiabatic shear bands in Ta and Ta-W alloys, *Acta Mater.* 49 (2001) 2905-2917.
- [42] T. Sakai, M. Ohashi, K. Chiba, J. Jonas, Recovery and recrystallization of polycrystalline nickel after hot working, *Acta Metall.* 36 (1988) 1781-1790.
- [43] H. McQueen, The production and utility of recovered dislocation substructures, *Metall. Trans. A*. 8 (1977) 807-824.
- [44] J. Bailey, P. Hirsch, The recrystallization process in some polycrystalline metals, In *Proceedings of the Royal Society of London A: Math. Phys. Eng. Sci.* 267 (1962) 11-30.
- [45] J.C. Li, Possibility of subgrain rotation during recrystallization, *J. Appl. Phys.* 33 (1962) 2958-2965.
- [46] Y. Wang, W. Shao, L. Zhen, X. Zhang, Microstructure evolution during dynamic recrystallization of hot deformed superalloy 718, *Mater. Sci. Eng. A*. 486 (2008) 321-332.
- [47] J. Hines, K. Vecchio, Recrystallization kinetics within adiabatic shear bands, *Acta Mater.* 45 (1997) 635-649.
- [48] J.A. Hines, K.S. Vecchio, S. Ahzi, A model for microstructure evolution in adiabatic shear bands, *Metall. Mater. Trans. A*. 29 (1998) 191-203.

- [49] M. Meyers, Y. Xu, Q. Xue, M. Perez-Prado, T. McNelley, Microstructural evolution in adiabatic shear localization in stainless steel, *Acta Mater.* 51 (2003) 1307-1325.
- [50] R.D. Doherty, Recrystallization and texture, *Prog. Mater. Sci.* 42 (1997) 39-58.
- [51] D. Hughes, N. Hansen, High angle boundaries formed by grain subdivision mechanisms, *Acta Mater.* 45 (1997) 3871-3886.
- [52] M. Sundararaman, P. Mukhopadhyay, S. Banerjee, Deformation behaviour of γ' strengthened Inconel 718, *Acta Metall.* 36 (1988) 847-864.
- [53] M. Miller, S. Babu, M. Burke, Intragranular precipitation in alloy 718, *Mater. Sci. Eng. A.* 270 (1999) 14-18.
- [54] T. Alam, M. Chaturvedi, S.P. Ringer, J.M. Cairney, Precipitation and clustering in the early stages of ageing in Inconel 718, *Mater. Sci. Eng. A.* 527 (2010) 7770-7774.
- [55] R. M'Saoubi, D. Axinte, C. Herbert, M. Hardy, P. Salmon, Surface integrity of nickel-based alloys subjected to severe plastic deformation by abusive drilling, *CIRP Annals-Manuf. Technol.* 63 (2014) 61-64.
- [56] J. Schiøtz, K.W. Jacobsen, A maximum in the strength of nanocrystalline copper, *Sci.* 301 (2003) 1357-1359.
- [57] A. Latapie, D. Farkas, Molecular dynamics investigation of the fracture behavior of nanocrystalline α -Fe, *Phys. Rev. B.* 69 (2004) 134110.

Table 1. Chemical composition in wt.% of the Inconel 718 disc forging.

	Fe	Ni	Cr	Mo	Nb	Ti	Al	C
Min. (%)	Bal.	50	17	2.8	4.75	0.65	0.2	
Max. (%)		55	21	3.3	5.5	1.15	0.8	0.08

Table 2. Main ideal orientations in simple shear deformation of face-centered cubic (FCC) materials [30].

Texture comp.	$\{h\ k\ l\}\langle u\ v\ w\rangle$	Euler angles ($^{\circ}$) ^a		
		Φ_1	Φ	Φ_2
A_1^*	(111)[-1-12]	35.26/215.26	45	0/90
		125.26/305.26	90	45
A_2^*	(111)[11-2]	144.74/324.74	45	0/90
		54.74/234.74	90	45
A	(1-11)[110]	0	35.26	45
\bar{A}	(-11-1)[-1-10]	180	35.26	45
B	(1-12)[110]	0/120/240	54.74	45
\bar{B}	(-11-2)[-1-10]	60/180/300	54.74	45
C	$\{001\}\langle 110\rangle$	90/270	45	0/90
		0/180	90	45

^a Given in the $\phi_2 = 0^{\circ}, 45^{\circ}$ and 90° sections.

Table 3. Chemical composition (at.%) of the Al-rich and Nb-rich clusters in the surface white layer in comparison with that measured on γ' and γ'' precipitates in the undeformed bulk material.

		Ni	Cr	Fe	Co	Mo	Nb	Al	Ti
White layer	Al-rich cluster	65.6±1.1	5.3±0.5	5.3±0.5	0.1±0.1	0.4±0.1	6.6±0.7	10.0±0.7	6.2±0.5
	Nb-rich cluster	67.4±0.9	2.3±0.4	2.1±0.4	0.2±0.2	1.8±0.3	20.3±0.9	1.1±0.3	4.6±0.5
Bulk	γ' precipitate	71.4±0.6	0.3±0.1	1.6±0.1	1.8±0.1	1.7±0.1	3.9±0.3	10.5±0.3	8.5±0.3
	γ'' precipitate	68.7±0.2	2.3±0.1	2.2±0.1	1.6±0.1	2.0±0.1	16.8±0.2	0.6±0.1	4.5±0.1

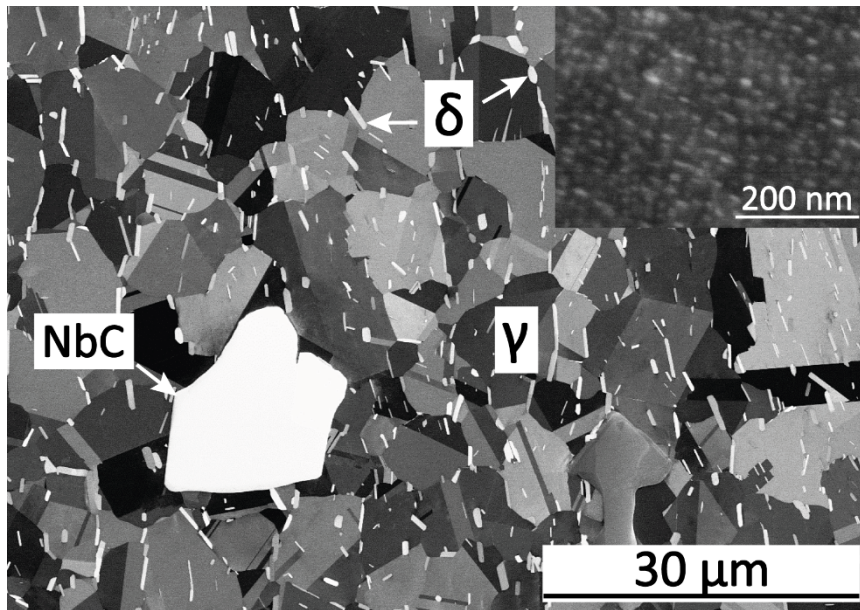


Fig. 1. Electron channeling contrast image (ECCI) showing microstructure of the aged Inconel 718 forging. It consists of equiaxed grains of the γ matrix, δ platelets and primary carbides NbC. Insert showing dispersed γ' and γ'' precipitates in the γ grains.

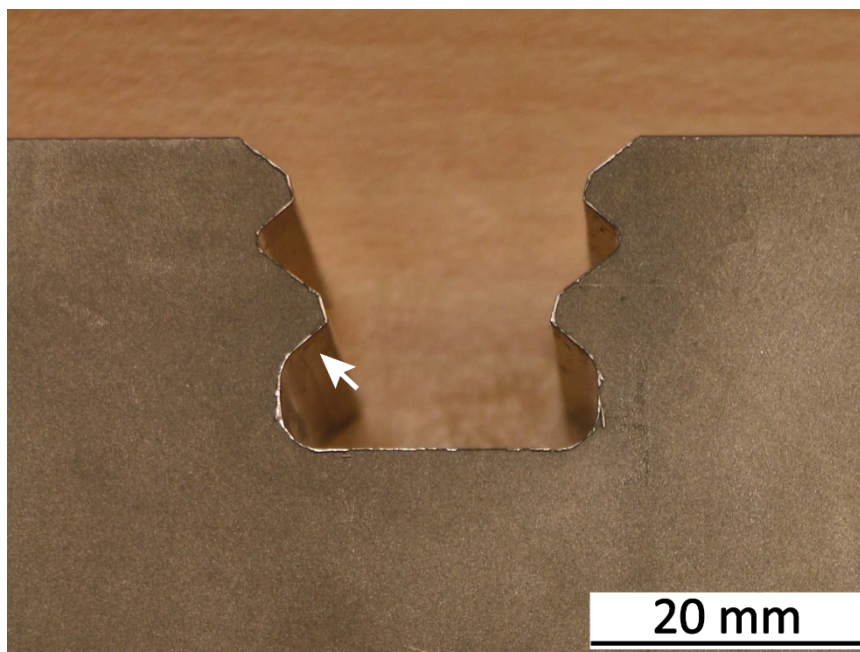


Fig. 2. Broached slot with a fir-tree profile and the white arrow points out the contact surface where the broached specimens were prepared.

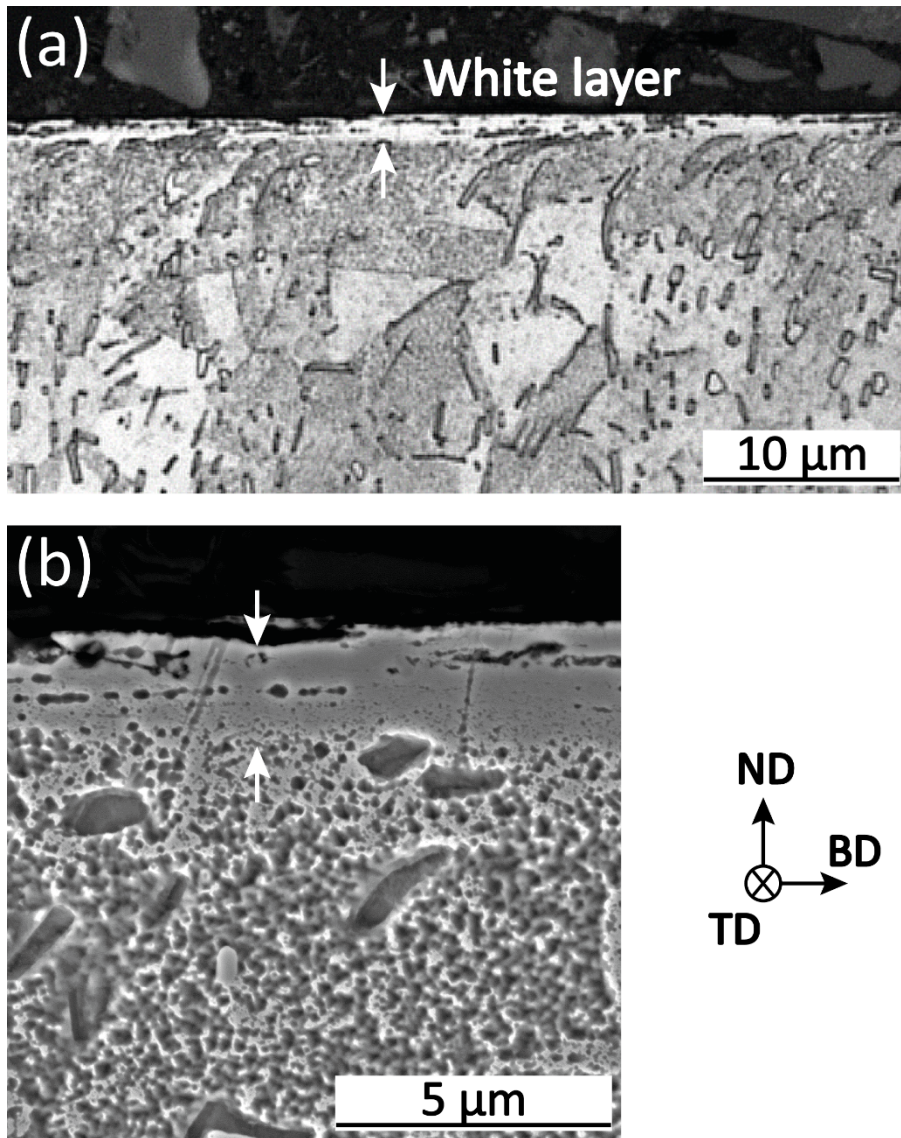


Fig. 3. (a) Optical micrograph of the etched cross section showing the appearance of a thin white layer. (b) SEM micrograph showing the high resistance of the white layer to etching. The schematic inset shows the broaching direction (BD), transverse direction (TD) and normal direction (ND) in the micrographs.

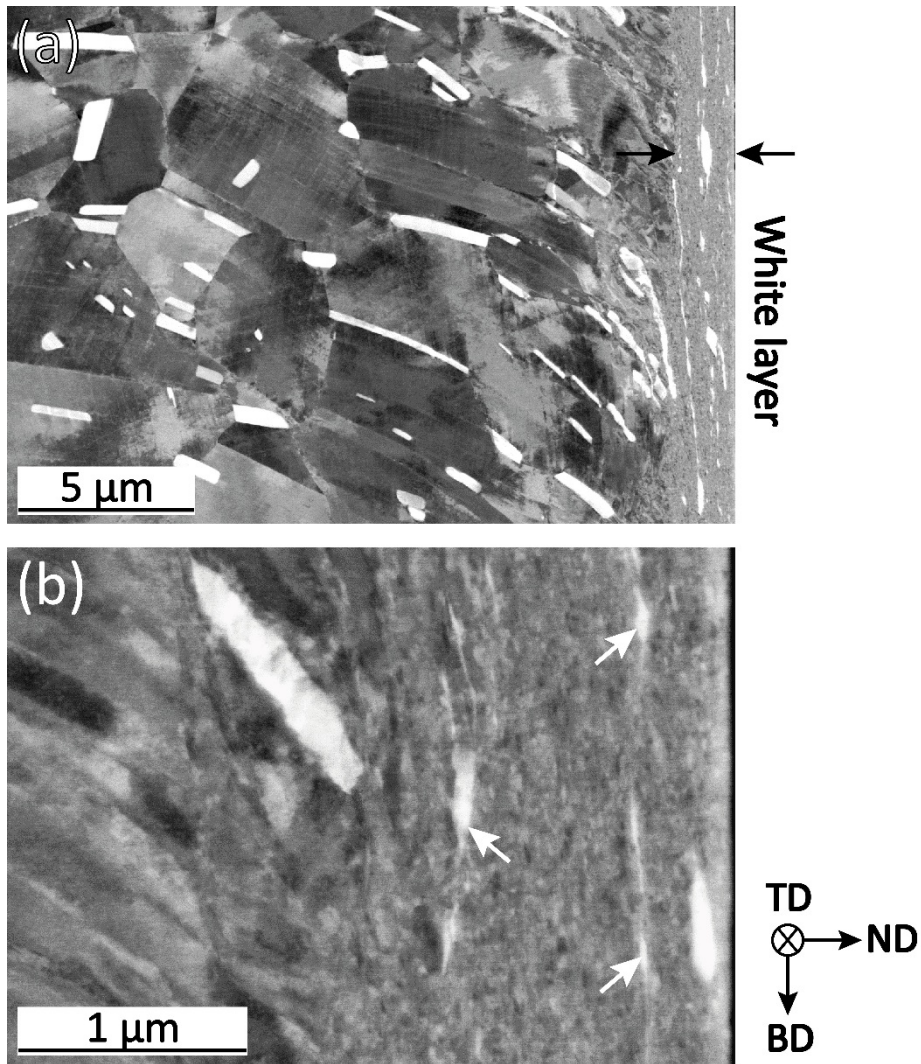


Fig. 4. ECCI micrographs: (a) the highly deformed microstructure beneath the broached surface; (b) δ fragmentation within the surface white layer due to deformation breakage, some δ fragments are pointed out by white arrows. The schematic inset shows the broaching direction (BD), transverse direction (TD) and normal direction (ND) in the micrographs.

Broached surface

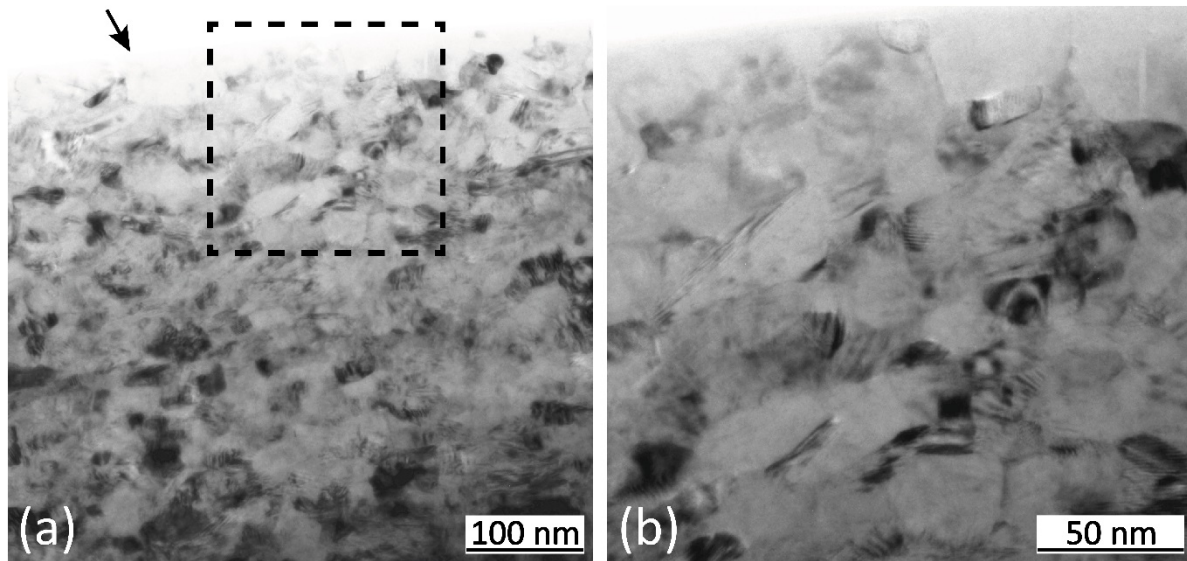


Fig. 5. TEM bright-field micrographs from the broached white layer showing the ultra-fine structure with nano-sized grains: (a) overview; (b) the majority of the grains are in the range of 20 nm to 50 nm. The foil plane is the transverse-normal plane.

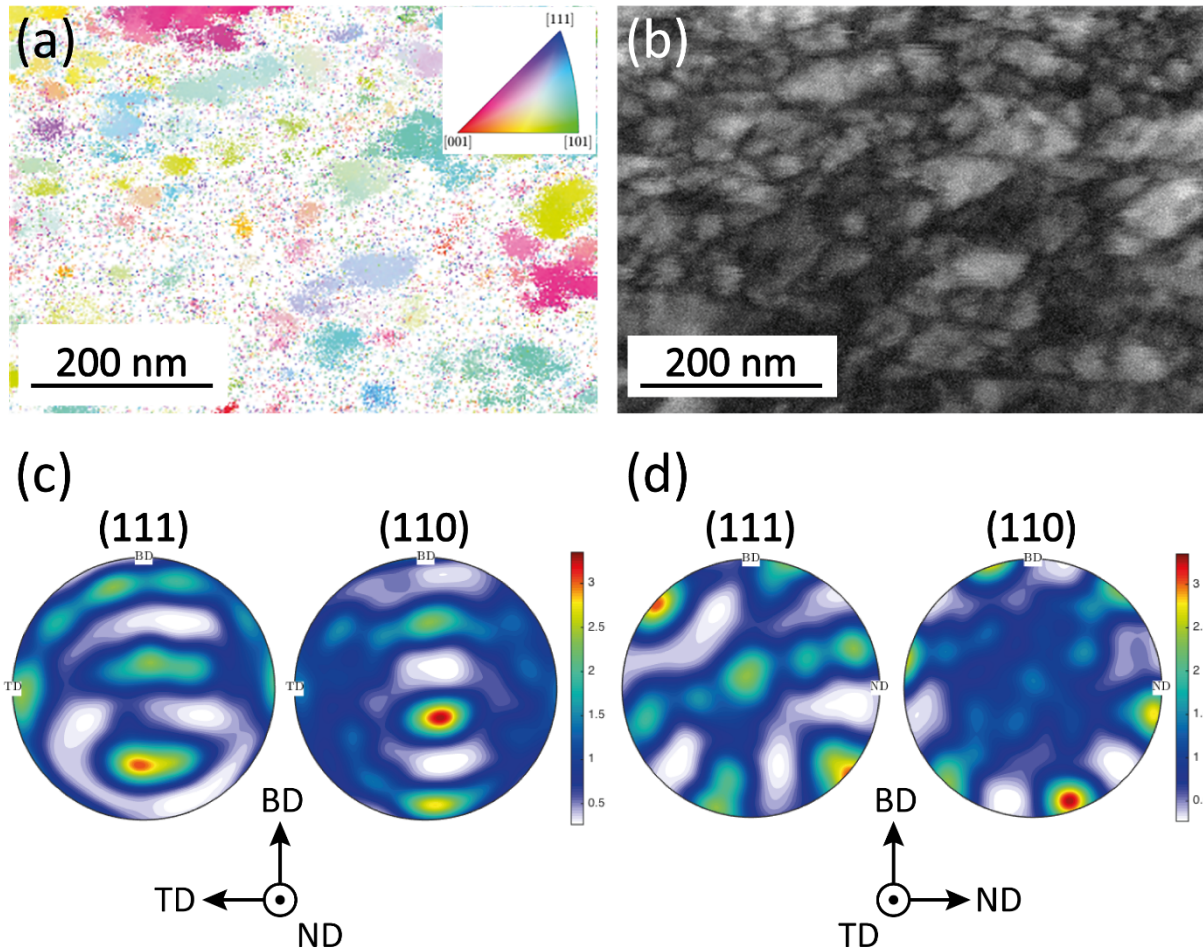


Fig. 6. (a) TKD inverse pole figure (IPF) map, with color representing crystallographic direction parallel to the broaching direction (horizontal in figure) and (b) corresponding band contrast map. The thin foil was taken from the surface white layer in the broaching-transverse plane. The corresponding (111) and (110) pole figures, collected from the sample plane (c) and the 90° rotational plane, i.e. broaching-normal plane (d), show a shear deformation induced texture. The broaching direction (BD), transverse direction (TD) and normal direction (ND) in the pole figures have been depicted.

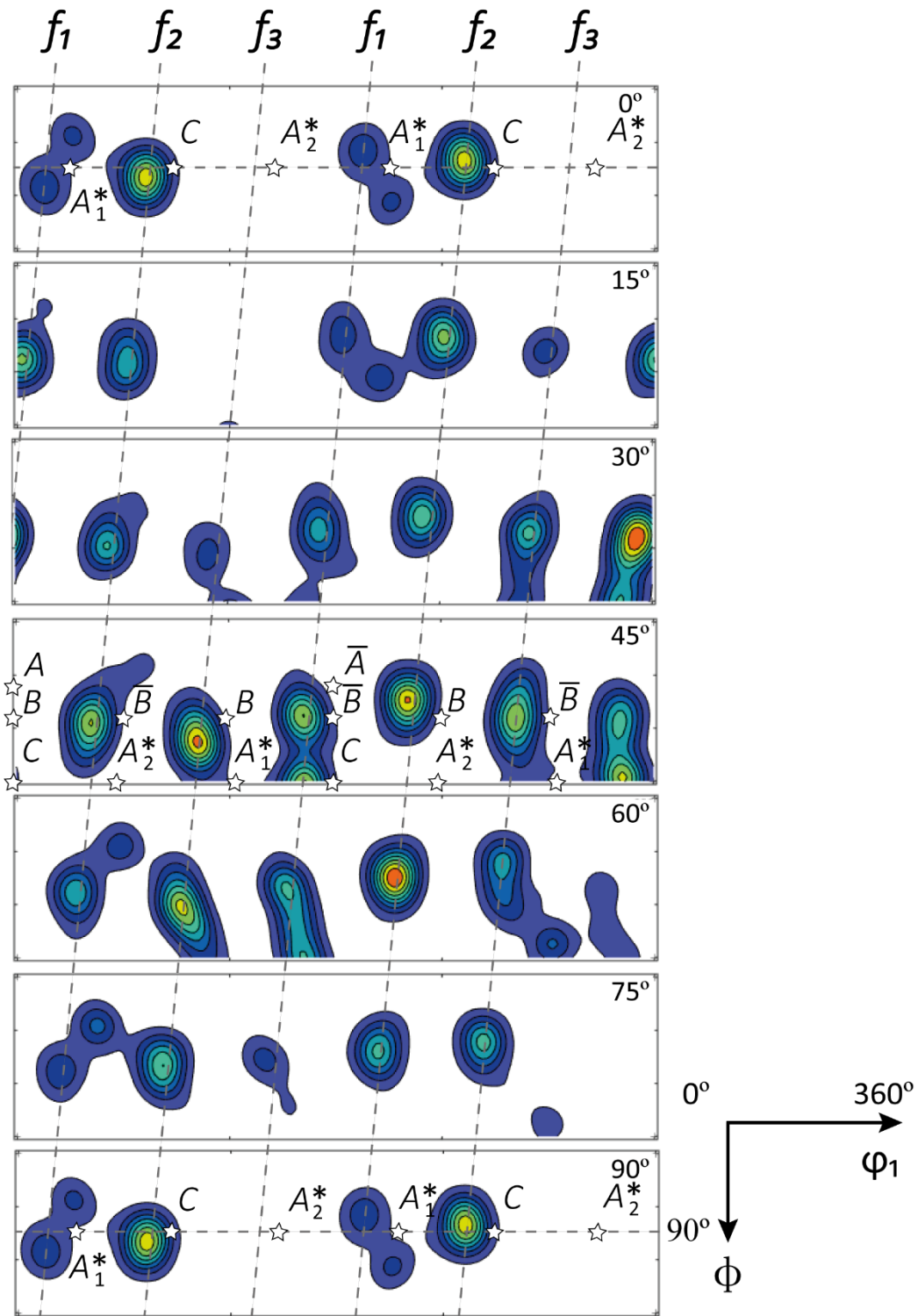


Fig. 7. $\phi_2 = \text{constant}$ (0° to 90° in steps of 15°) sections of the orientation distribution function (ODF) corresponding to Fig. 6(d). The main ideal orientations in simple shear deformation of face-centered cubic materials, as given in Table 2, are marked on the sections. Dash lines are depicted following the orientation concentrations which show three dominant fibers, designated as f_1 , f_2 and f_3 .

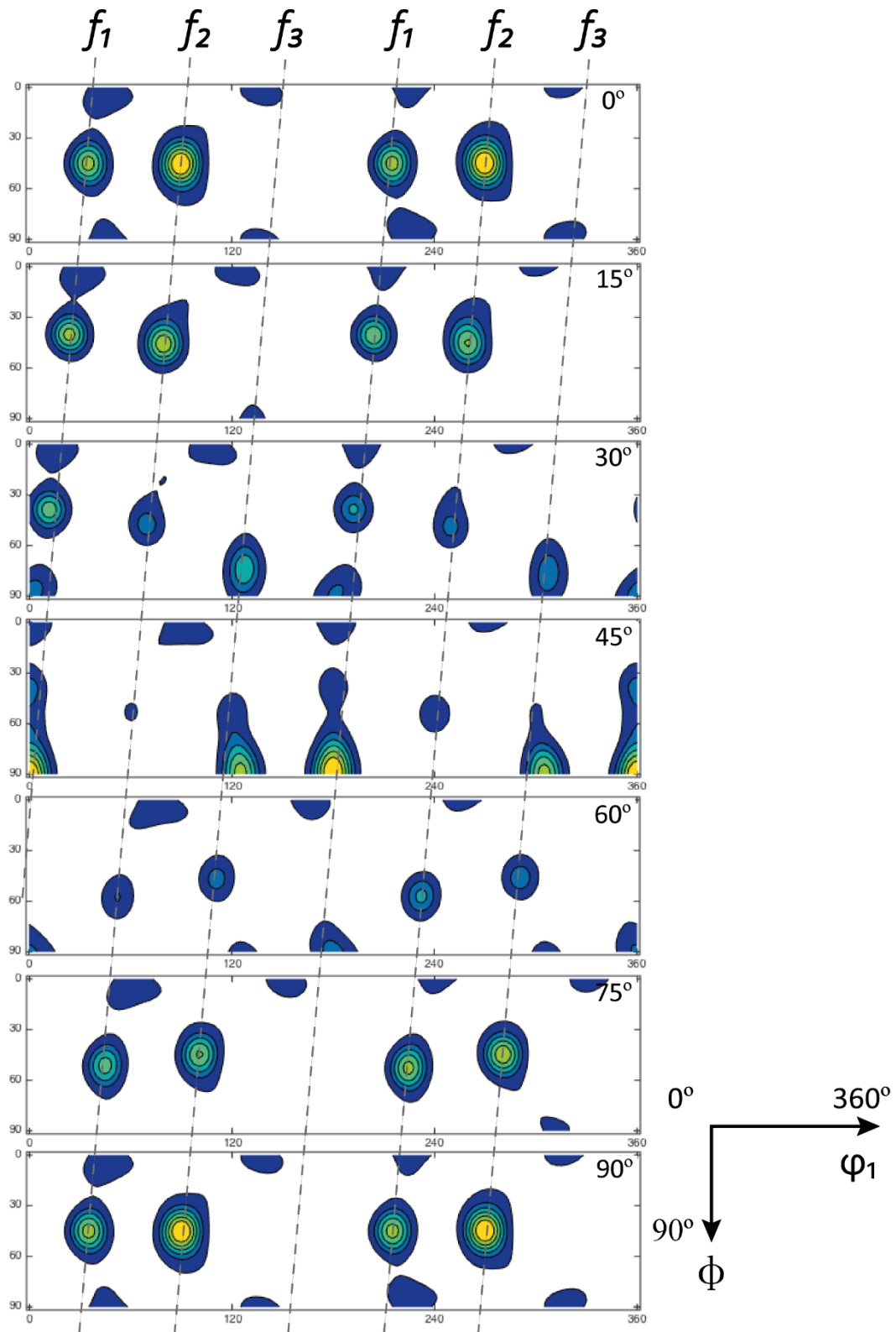


Fig. 8. $\phi_2 = \text{constant}$ ODF sections after simple shear deformation to a shear strain $\gamma = 4$, obtained from visco-plastic self-consistent (VPSC) simulation (1000 grains, starting from uniform texture) using secant interaction model. The three dominant fibers f_1, f_2 and f_3 that have been identified in the experimentally observed texture were successfully reproduced by VPSC simulations, see dash lines.

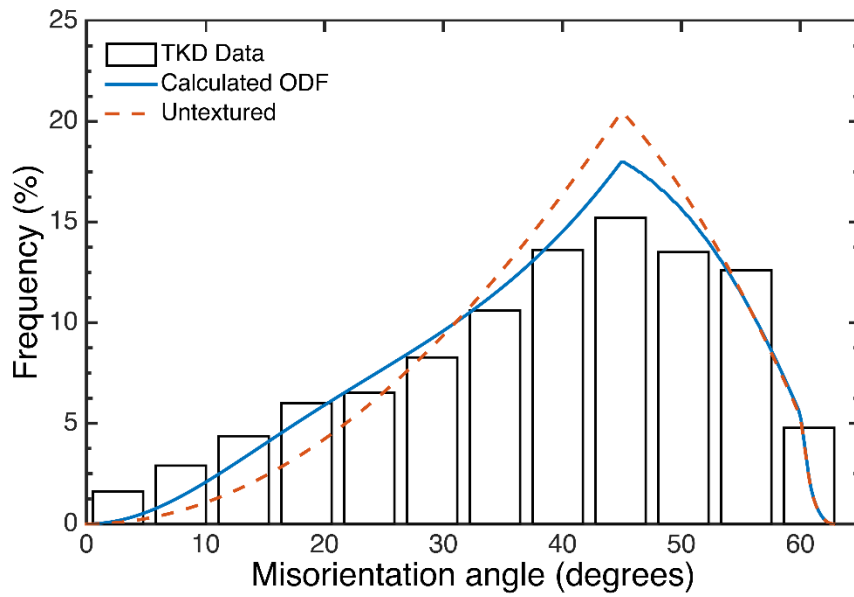


Fig. 9. Uncorrelated misorientation distribution histogram within the region examined by TKD. Uncorrelated misorientation distribution derived from the ODF corresponding to Fig. 7 (solid line) and Mackenzie distribution [33] for a FCC polycrystal with random textures (dash line) are also plotted for comparison.

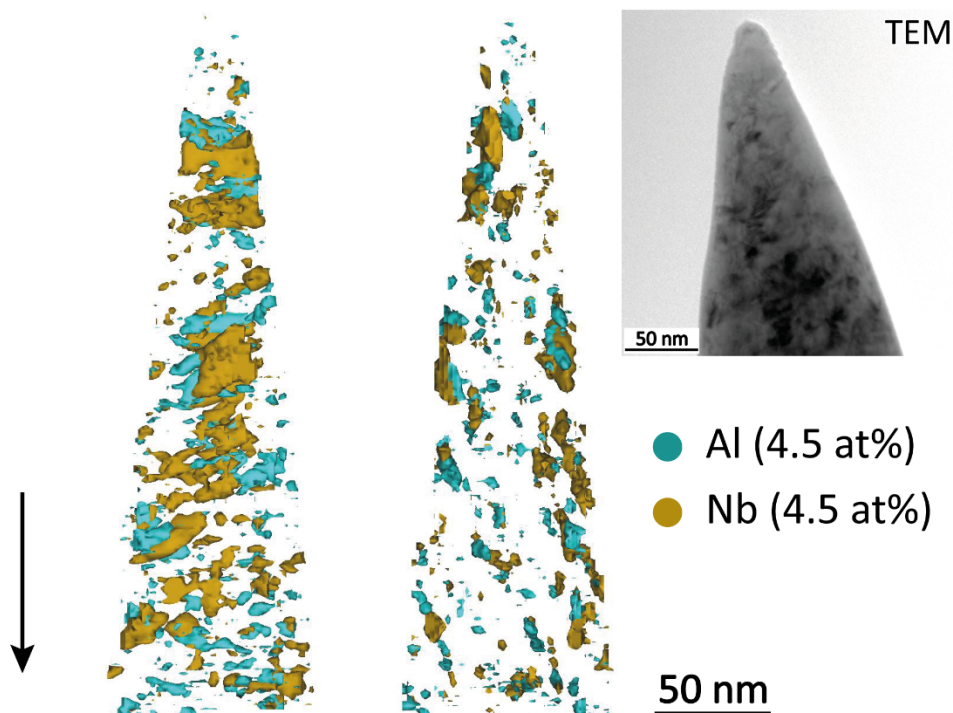


Fig. 10. Two views of an atom probe reconstruction with 90° rotation around the long axis of the needle. The isosurfaces reconstructed corresponding to 4.5 at.% of Al and Nb show the presence of nano-sized Al-rich and Nb-rich clusters in the broached white layer, aligned in one direction. The needles were lift-out in the broaching-transverse plane and the analysis direction, as pointed out by the arrow, is in the transverse direction. The bright-field TEM micrograph confirms the nano-crystalline structure.

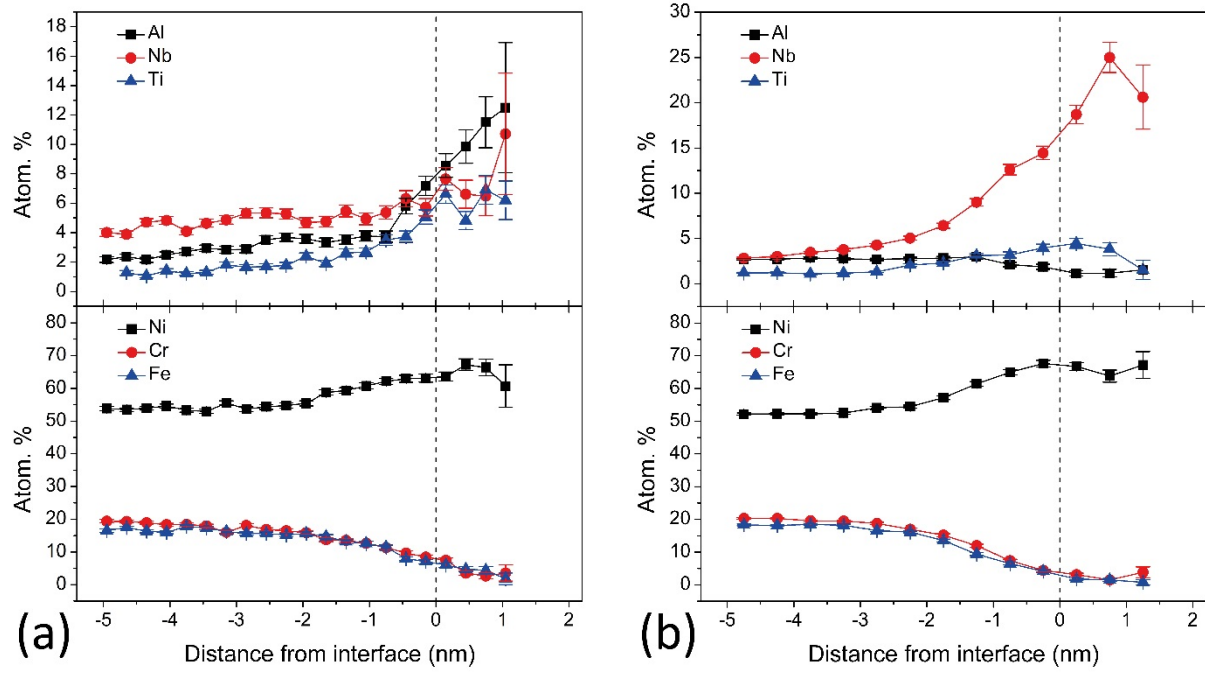


Fig. 11. Proxigrams showing the chemical composition changes across the interface (zero position as indicated by dash lines) between the clusters and the γ matrix (a) Al-rich clusters; (b) Nb-rich clusters.

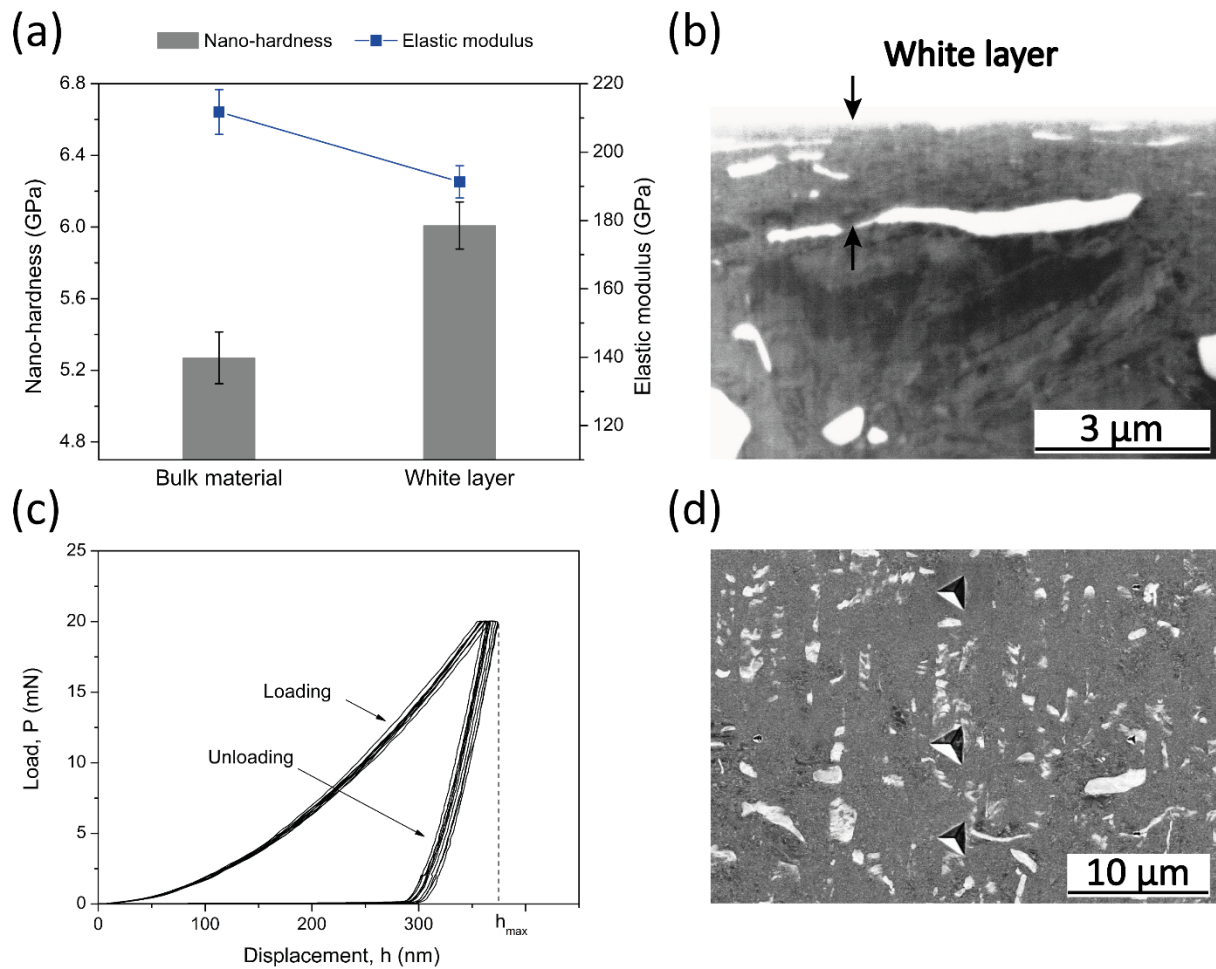


Fig. 12. (a) A comparison of the distinct mechanical properties of the broached white layer from the undeformed bulk material. (b) Cross sectional observation from the notch prepared by FIB showing the thickness of the residual white layer after polishing. (c) Recorded load versus displacement curves showing the maximum penetration depth (h_{max}) of the indenter when measuring on the surface white layer. (d) ECCI micrograph where one can see examples of the symmetrical triangle-shaped indents made from the top of the broached surface.

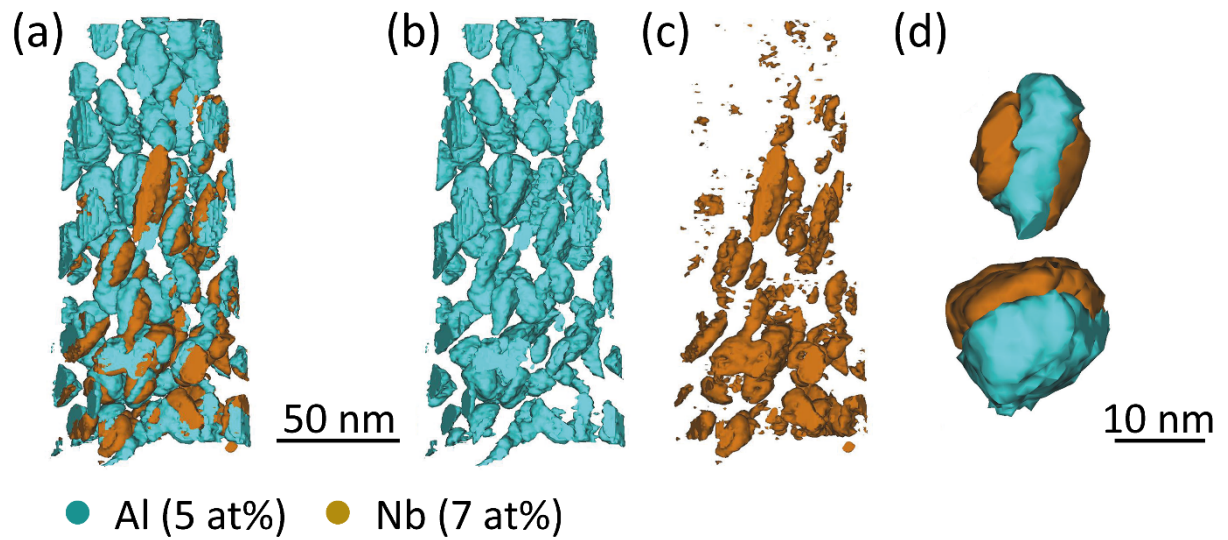


Fig. 13. APT reconstructions from the undeformed bulk. (a) Isosurfaces corresponding to 5 at.% Al and to 7 at.% Nb. (b) and (c) show the different isosurfaces in (a) in separate figures. (d) Magnified examples of co-precipitation from (a)